Contents list available at IJRED website

Int. Journal of Renewable Energy Development (IJRED)

Journal homepage: http://ejournal.undip.ac.id/index.php/ijred

Research Article

Movement of a Solar Electric Vehicle Controlled by ANN-based DTC in Hot Climate Regions

Asma Benayed[a*], Brahim Gasbaoui[b], Said Bentouba[a], Mohammed Amine Soumeur[b]

[a*]*Department of Renewable Energy and Hydrocarbure, African University Ahmed Draia - Adrar, Adrar, 01000, Algeria.*

[b]*Laboratory of Smart Grid Renewable Energy (SGRE), Faculty of Technology, Department of Electrical Engineering, Bechar University, B.P. 417, 0800, Algeria.*

ABSTRACT. Vehicle autonomy presents the most complex problem for modern commercialized solar electric vehicle (SEV) propulsion systems. The power supplied by electric vehicles' batteries is limited by the state of charge, the type of battery, and its level of technological development. This study's aim was to resolve the problem of energy variation at several velocities and under different road topology conditions. Several works related to the use of fuzzy logic confirm that classical regulators have such advantages over fuzzy regulators as short processing times and mathematical precision. Therefore, the hybrid power source is presented as the best solution for energy management, and it is composed of a solar panel (PV) and a nickel metal hydride battery. The PV system is connected to the SEV via a boost converter that is controlled using the maximum power point tracking technique. In this paper, we used an intelligent PI regulator for direct torque control, which introduced a certain degree of intelligence into the regulation strategy. Indeed, this approach of associating the PI regulator with the fuzzy rules-composed supervisor allowed us to take advantage of both the PI's mathematical precision and the adaptability, flexibility, and simplicity of fuzzy linguistic formalism. Because of its dynamic capabilities, an adaptive PI regulator was substituted to achieve high speeds and a satisfactorily vigorous performance while quickly compensating for the disturbances that were expected to possibly take place on the regulation chain. The present study's results confirm that the proposed control approach increased the utility of SEV autonomy under several speed variations. Moreover, the industry's future offerings must take the option of hybrid power management into consideration during this type of vehicle's manufacturing phase.

Keywords: Solar Photovoltaic (PV), MMPT, Artificial Neural network, Buck Boost, DC–DC converter

Article History: Received: 20th April 2018; Revised: 14th September 2020; Accepted: 3rd October 2020; Available online: 6th Oct 2020
How to Cite This Article: Benayed, A.B., Gasbaoui, B., Bentouba, S., Soumeur, M.A. (2021) Movement of a Solar Electric Vehicle Controlled by ANN-based DTC in Hot Climate Regions. *International Journal of Renewable Energy Development*, 10(1), 61-70.
https://doi.org/10.14710/ijred.2021.18596

1. Introduction

Due to its effect on every aspect of our lives, from heating, air conditioning, food preparation, transportation, and power production, energy is one of humankind's most vital necessities. Both traditional and renewable sources of energy themselves cannot be utilized to do research, as they are converted into heat, mechanical, or electrical energy (Ghosh *et al.* 2009).

Photovoltaic (PV) energy is, as a matter of fact, the cleanest technology used in the world. Its main disadvantage, however, is its poor efficiency. A variety of solutions to this have been proposed, including hybrid systems (Ammari *et al.* 2017), optimization (Kumar *et al.* 2016), and control algorithms (Javed *et al.* 2018), which were developed to optimize the performance of the PV generator.

Algeria has one of the world's highest solar capacities with 2,000 h per year across the entire country (but over 3,900 h in the highlands and the Sahara). The global horizontal irradiation is 3,000 Wh/m² annually in the north and more than 5,000 Wh/m² annually in the south (i.e., the Sahara) (Belatrache *et al.* 2017).

Because they guarantee energy supply stability and increase device reliability, energy storage systems are important for power system operations, and they come in widely varying shapes and sizes. Nickel metal hydride (NiMH) batteries have dominated in automotive applications since the 1990s due to their overall performance and their offering of the best available combination of power energy density, thermal performance, lifecycle, and low maintenance cost (Mebarki *et al.* 2017).

The artificial neural network-based direct torque control (ANN-DTC) strategy is one kind of high-performance driving technology used for AC motors due to its simple structure, and its ability to achieve a fast response of flux and torque has attracted growing interest in recent years. Using PI-controlled ANN-DTC without a hysteresis band can effectively reduce torque and flux ripple, enhance the system's robustness, and improve its dynamical performance. A DC–DC converter is used with a control strategy to ensure that a solar electric vehicle's (SEV) energy requirements are met. This paper presents an SEV using a hybrid PV–battery energy storage power

* Corresponding author: asma.amal70@yahoo.fr

system, which required that it use ANN-based direct torque under speed variation. In this study, the nickel metal hybrid batteries would charge using a PV system; when the battery's state of charge fell below the reference state of charge, the PV would distribute its power between the battery and the SEV. The battery would then discharge, feeding the proposed propulsion system when the battery's state of charge became higher than the reference state of charge (Jia-Min *et al.* 2014; Gasbaoui *et al.* 2012). This paper deals with the behavior of the SEV's movement in hot weather and at different speeds. The SEV was equipped with two 3.3 HP induction motors, and an ANN-DTC was proposed to minimize current ripple, flux, and electromagnetic torque in both. To evaluate the performance of the proposed system, a simulation was performed on all the system's operating conditions.

This paper is organized as follows. Section 2 presents the SEV model. Section 3 deals with the specifics of the ANN-DTC. Section 4 contains a description of the system and the control. Section 5 presents, and then discusses, the results of the simulation. Finally, a conclusion is reached.

2. Solar Electric Vehicle Model

The resistive forces that apply to the solar car's movement are (Fig. 1):

- the rolling resistance force "F_{tire}" due to the friction of the tires on the road;
- the aerodynamic drag force "F_{aero}" caused by the friction of the body moving through the air; and
- the climbing force "F_{slope}" that is needed on a sloped road.

The globally resistive force "F_r" is the sum of all the previously mentioned resistive forces, as shown in Equation 1 (Yang and Lo 2008; Gao and He 2008):

$$F_r = F_{tire} + F_{aero} + F_{slope} \quad (1)$$

The rolling resistance force is described as:

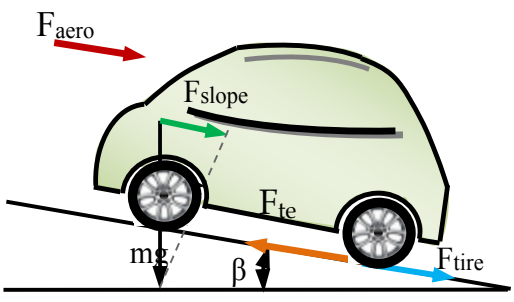

Fig. 1. The forces acting on a vehicle moving along a slope.

Table 1
Parameters of the electric vehicle model

R	0.28 m	Af	2.60 m²
M	550 Kg	Cd	0.32
Fr	0.01	ρair	1.2 Kg/m³

$$F_{tire} = mgf_r. \quad (2)$$

The aerodynamic resistance force is described as:

$$F_{aero} = \frac{1}{2}\rho_{air}A_f C_d v^2 \quad (3)$$

Where "m" is the vehicle's total mass, "f" is the rolling resistance force constant, "g" is the acceleration due to gravity, "ρ_{air}" is air density, "C_d" is the aerodynamic drag coefficient, "A_f" is the frontal surface area of the vehicle, "v" is the vehicle's velocity, and "ß" is the road slope angle. The values of these parameters are shown in Table 1.

The weight parameter of the SEV can be obtained adding the weight of the specific components (PV panels, battery pack, electric motor, and inverter). The solar vehicle considered in this work has separate induction motors.

3. Artificial Neural Network-Based Direct Torque Controller

The basic DTC strategy is based on the determination of instantaneous space vectors in each sampling period regarding desired flux and torque references. The reference speed is compared to the measured one, and the error thus obtained is applied to the speed regulator PI, whose output yields the reference torque (Ouledali *et al.* 2019).

An artificial neural network (ANN) is based on learning by decreasing errors during a training period; once training has been completed, the objective functions should be optimized (Devi *et al.* 2016; Siva *et al.* 2017; Chill and Lin 2006; Sasikumar and Harinandan 2014).

The induction motor's stator flux can be estimated using the following equations:

$$\phi_{ds} = \int_0^t (V_{ds} - R_s i_{ds})dt \quad (4)$$

$$\phi_{qs} = \int_0^t (V_{qs} - R_s i_{qs})dt \quad (5)$$

$$|\phi_s| = \sqrt{\phi_{ds}^2 + \phi_{qs}^2} \quad (6)$$

$$\theta_s = \tan^{-1}\left(\frac{\phi_{qs}}{\phi_{ds}}\right) \quad (7)$$

The electromagnetic torque T_{em} can be described as follows:

$$T_{em} = \frac{3}{2} p(\phi_{ds} i_{qs} - \phi_{qs} i_{ds}) \quad (8)$$

The neural network used in this study was based on three inputs: flux, torque, and sector. The network employed was a 3-5-3 feedforward network with a log sigmoid transfer function at its first layer, a hyperbolic tangent sigmoid transfer function at its second, and a linear transfer function at its third. All three neural networks were trained perform to at 0.00001 msec. A Levenberg–Marquardt backpropagation algorithm was used to train the neural networks, updating weights and bias values according to the Levenberg–Marquardt optimization (Fig. 2).

The neural network inputs resulted in an error between the estimated flux value and its reference value; the difference between the estimated electromagnetic torque, the torque reference, and the position of the flux stator vector was represented by the number of the corresponding sector. The neural network output layer was composed of three neurons.

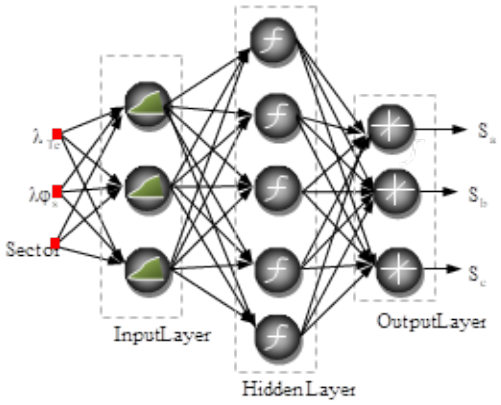

Fig. 2. Schema of artificial neural network switching.

4. System and Control Description

The SEVs included PV panels to generate electricity and feed the NiMH batteries and induction motors. Batteries were included in case the PV panels failed to supply the induction motors. A bidirectional converter was used to transfer and regulate the energy traveling from the generators (i.e., the PV panels and the batteries) to the induction motors. The two induction motors were coupled with the left and right rear wheels.

Power generated from the PV array was transmitted to the motor and the battery via a DC–DC boost converter and controlled using incremental conductance maximum power point tracking (MPPT) algorithm. (Gasbaoui *et al.* 2013). A bidirectional DC–DC converter was used to mitigate power disturbances between the battery and the PV panel. The two rear induction motors were controlled by an ANN-DTC using an adaptive fuzzy speed controller (Allaoua *et al.* 2013; Zhang *et al.* 2003). The electronic differential system ensured robust vehicle control on different road topologies. The basic principles of energy management employed in this study are shown in Fig. 3. A block diagram of the ANN-DTC and the differential electronics (Moreno *et al.* 2006) is shown in Fig. 4.

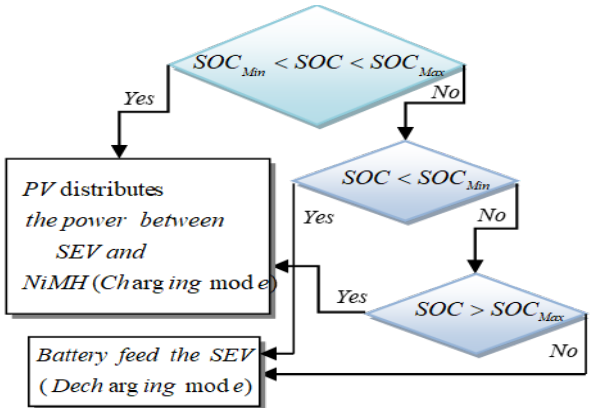

Fig. 3. Diagram of the proposed energy policy for the SEV.

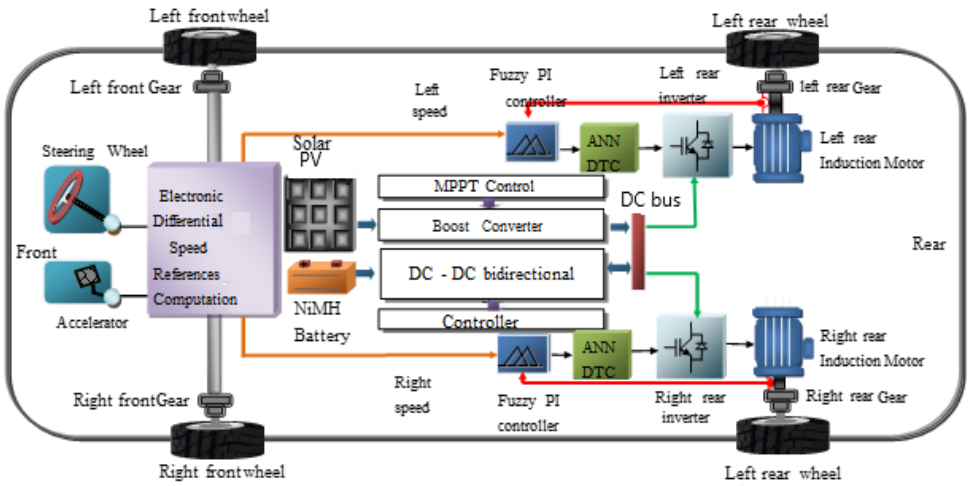

Fig. 4. SEV control system.

5. Simulation Results and Discussion

5.1. Nickel Metal Hydride Battery power responses.

To characterize the SEV's behavior, simulations were performed using a model (Fig.4) in a MATLAB/SIMULINK environment. The simulation was divided into two phases. The first phase comprised a performance test of the SEV controlled by an ANN-DTC, and the second phase tested the performance of the NiMH batteries and PV panels under different conditions (Tahiri *et al*. 2019).

The topology test was subdivided into three phases (Fig. 5). In the first, the SEV traveled along a straight road at 20 km/h. The solar irradiance was 1,000 W/m², and the temperature was 25°C. The second phase was the SEV accelerate to 40 km/h, and the temperature was increased steadily to 50°C, while the solar irradiance was ramped down from 1,000 to 190 W/m², with MPPT continuously tracking the maximum power and solar irradiance. The final phase was the SEV traveling in the hottest region. The SEV decelerated to 30 km/h, the solar irradiance was restored to 1,000 W/m², and the temperature was increased to 50°C. The road topologies at each phase are illustrated in Fig. 5, and the speed constraints at each phase are shown in Table 2.

Table 2
Specified road topologies.

Phases	Event information	Vehicle speed (km/h)
Phase 1	Bridge, Break	20
Phase 2	Acceleration	40
Phase 3	Deceleration	30

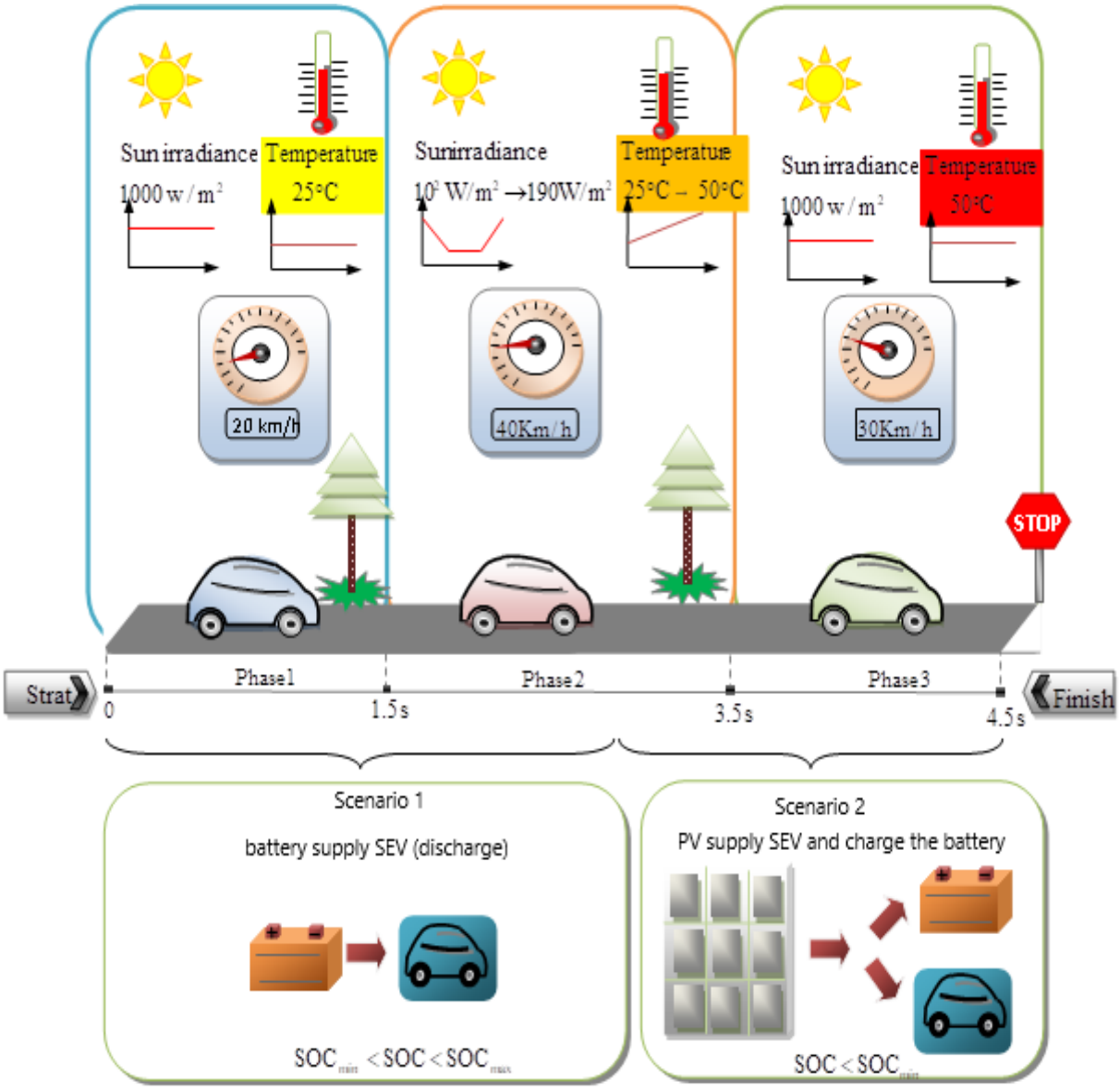

Fig. 5. Driving scenarios under the hottest region's conditions.

As described above, the SEV traveled along a straight road during the first phase at 20 km/h under a solar irradiance of 1,000 W/m² and a temperature of 25°C (Fig. 6). The second phase was an increase in temperature, but the SEV's linear speed was not affected, demonstrating the same robustness of both the control and the driving wheels. Finally, as the SEV traveled in the hottest region, the temperature and solar irradiance reached 50°C and 1,000 W/m², respectively, and the vehicles decelerated to 30 km/h (Fig. 7).

Figure 8 and Table 3 note that the effect of the disturbance was ignored by the adaptive fuzzy PI controllers, affording better performance in both overshoot control and tracking error.

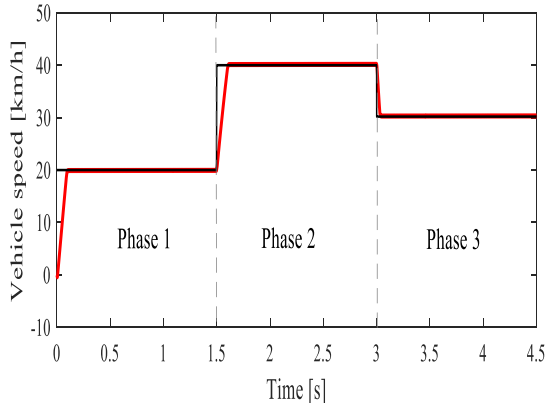

Fig. 6. Variation of vehicle speed in different phases.

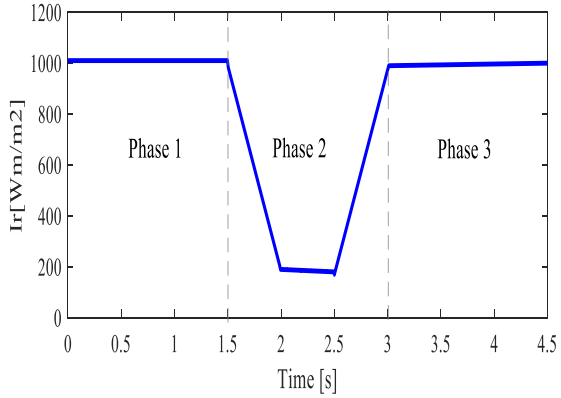

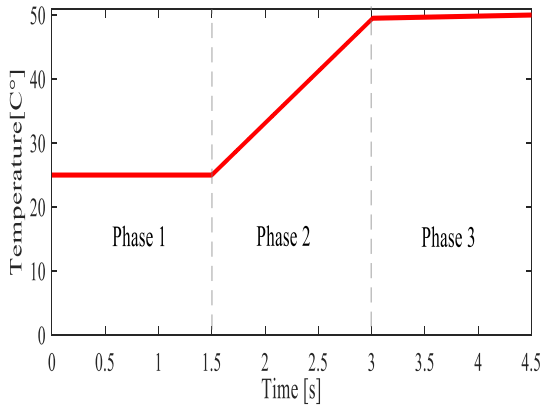

Fig. 7. (a): Variation of irradiance in different phases; **(b):** variation of temperature in different phases.

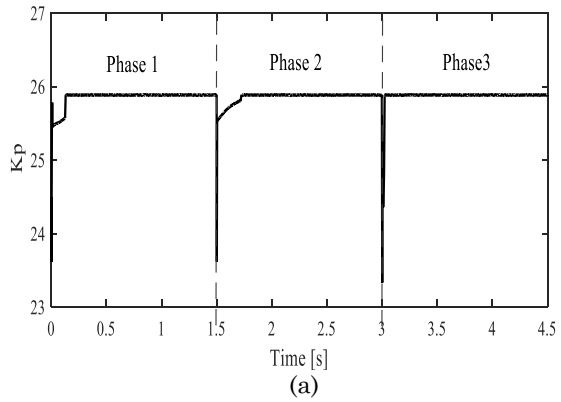

(a)

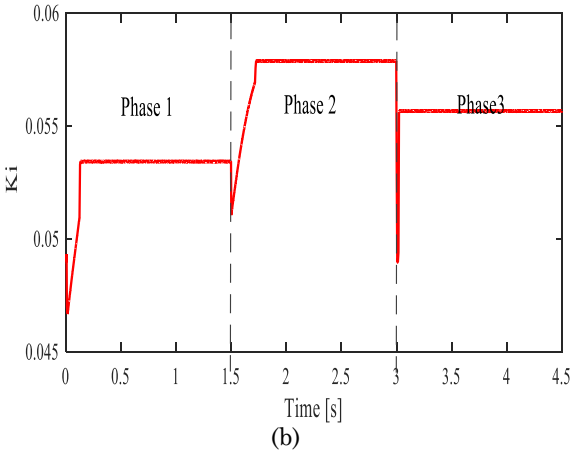

(b)

Fig. 8. (a): Variation of gain kp of adaptive fuzzy speed PI controller; **(b):** variation of gain ki of adaptive fuzzy speed PI controller.

Table 3
PI and fuzzy logic controllers' speed responses.

Results	Rising time (s)	Overtaking (%)	Steady state error (%)
Fuzzy PI speed controller	0.1272	0.00	2.7e-5

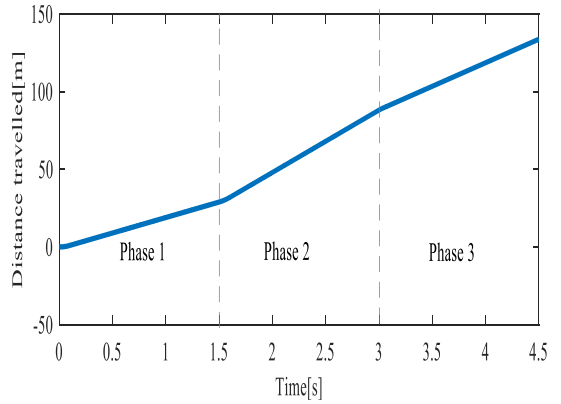

Fig. 9. Evaluation of distance traveled at different speeds.

Figure 9 reflects the relationship between the vehicle's change in speed and the distance traveled in the different phases; for this, a new fitting formula was developed:

$$d_{traveled}[m] = -0.45t^3 + 3.6t^2 + 0.85t + 0.67 \quad (9)$$

The SEV required a current of 12.40 A in the first phase for the tow induction motors, yielding a driving force of 74.30 N.

In the second phases, the effect of acceleration with 40 km/h on the directly road has been obtained. The wheels' driving force increased, and the current demand doubled from the current braking phase, causing the PV panel and NiMH battery to exploit 80% of their capacity to achieve the power necessary to negotiate the road's condition, which can be interpreted physically by the increase in the vehicle's overall resistive torque (Table 4). However, the linear speeds of the two induction motors remained similar, and the lowering of the road's gradient did not influence the torque controller. In the third phase, the demands on both the current and driving force increased, indicating that the vehicle entered a recharging phase, which can be explained by the subsequent decrease in the current demand and driving force (Figs. 10 and 11). Finally, the current increased to 31.32 A, and the driving force increased to 83.20 N.

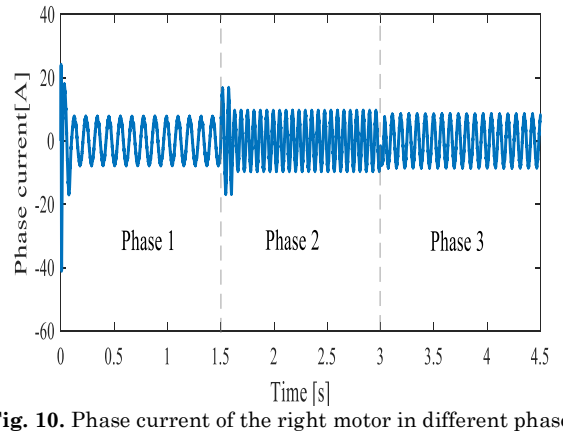

Fig. 10. Phase current of the right motor in different phases.

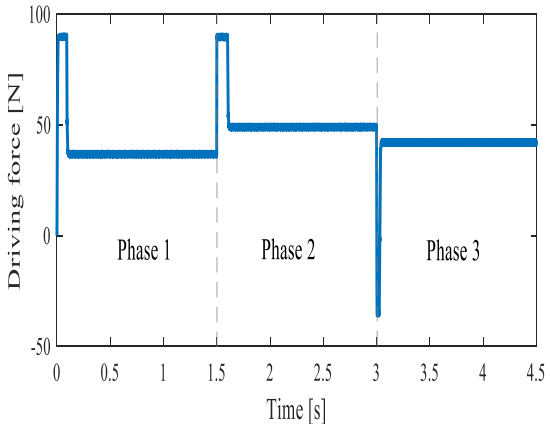

Fig. 11. Evaluation of the right motor's driving forces in different phases.

Table 4
Values of phase currents and driving forces in different phases.

Phases	Phase 1	Phase 2	Phase 3
Current of the right induction motor [A]	6.20	7.55	6.66
Current of the left induction motor [A]	6.20	7.55	6.66
Current of both induction motors [A]	12.40	15.10	13.32
Driving force of the right induction motor [N]	37.15	49.70	41.60
Driving force of the left induction motor [N]	37.15	49.70	41.60
Driving force of both induction motors [N]	74.30	98.40	83.20

In the first phase, the vehicle's resistive torque was 20.54 Nm, and power propulsion system resisting more than 66% from nominal motor torque. During the breaking phase (Phase 2), the rear wheels built up to fit the traction chain demand, which induced a resistive torque of 27.50 Nm. Our results confirm that the traction chain under acceleration exerted more force than in the first phase; the vehicle, while decelerating, required only half the energy needed for acceleration. Table 5 summarizes the above-mentioned results.

The battery was sufficient to supply the SEV with power in the beginning, accelerating, and decelerating phases, indicating that the peak power of the NiMH batteries must be greater than or equal to the peak power of the electric motors. Table 6 lists this battery's parameters.

The battery's power production depended solely on the electronic differential assigned to the state of the acceleration/deceleration driver, which can be illustrated by the current (see Fig. 12).

Table 5
Vehicle torque in different phases.

Phases	1	2	3
The vehicle's resistive torque (Nm)	20.54	27.50	23.40
The vehicle's global resistive torque (%) compared to nominal motor torque of 30.98 Nm	66.30%	88.76%	75.53 %

Table 6
NiMH battery's parameters.

Rated capacity	6.5 Ah
Nominal Voltage	200 V
Maximum Capacity	7 Ah
Nominal Discharge Current	1.3 A
Exponential Voltage	1.28 V
Internal Resistance	2 mΩ
Rated Capacity	6.5 Ah
Fully Charged voltage	235.59 V
Capacity and Nominal Voltage	6.25 Ah
Exponential zone [voltage capacity]	[216.94 V 1.3 Ah]

The state of the NiMH battery's charge changed during the driving cycle; it seems that the state of charge (SOC) decreased rapidly at the beginning, and it ranged between 67.93% and 70% throughout every phase, from beginning to end (Table 7).

Battery power was controlled by the bidirectional converter, which accurately distributed power during every phase. The buck boost converter was not only a robust converter that guaranteed the transmission of voltage, but it also demonstrated excellent battery recharge characteristics while decelerating. These advantages were noted when the speed increased from 20 km/h to 40 km/h and the demanded voltage remained stable at 450 V (Fig. 13).

5.2. Solar Photovoltaic Panel

The solar PV field was composed of six parallel of three series of connected cells. The PV field's total power was 8.01 kW. Table 8 lists the PV panel's parameters.

The voltage of photovoltaic panels took on a high value during the first phase due to the low speed (v = 20 km/h), decreasing slowly in Phase 2 when the SEV accelerated to 40 km/h and stabilizing at 140 V (Fig. 14 [a]). In first phase, the SEV moved slowly (20 km/h), consuming minimal current (10 A) and power (2 kW). As the vehicle's speed increased, (40 km/h), current consumption peaked at 25 A before the regulator stabilized consumption to 7 A. When the speed decreased, the current's maximum value was recorded at 30 A (Fig. 14 [b]).

Fig. 14 (c) shows that the first phase (between t = 0.5s and 1.5 s), characterized by a 20-km/h speed and 1,000-W/m² irradiation, caused a decrease in power due to the induction motor's consumption outpacing the PV panel's production. Between t = 0.15 s and 2.5 s, power decreased due to low solar irradiance (190 W/m²). However, by t = 2.5 s, the power began rising until t = 3 s due to increasing irradiance (1,000 W/m²), stabilizing from between t = 3 s and 4.5 s. The duty cycles increased during times of high consumption (i.e., Phase 2) and decreased when the vehicle moved more slowly, such as in Phase 3 (Fig. 14 [d]).

Table 9 presents the variation of temperature, solar radiation, PV voltage, and PV power output during the different phases. The PV panels generated 7.00 kW when the vehicle was moving in a hot region (50°C) from t = 3–4.5 s at 30 km/h under 1,000 W/m² irradiance. The maximum power recorded in the first phase was 8.00 kW.

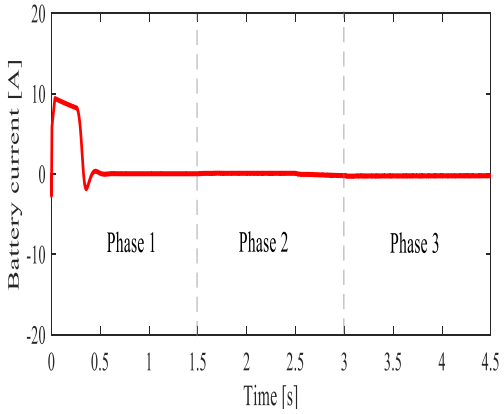

Fig. 12. Battery's current during the three phases.

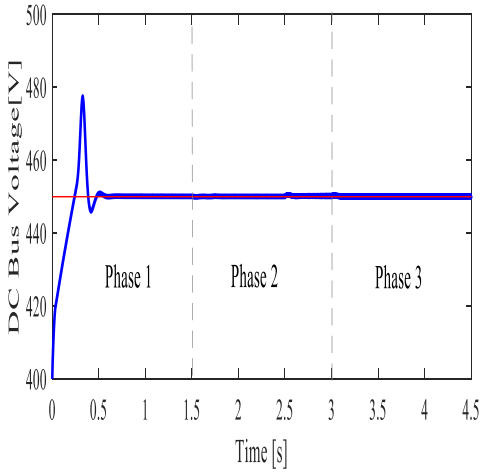

Fig. 13. Variation of DC bus voltage in different phases.

Table 7.
Evaluation of SOC (%) and power management of the power sources in the diverse speed variation.

Phase	Speed (km/h[s])	Begin phase (s)	End phase (s)	SOC begin	SOC end	SOC difference	Battery power	Observations
1	20	0	1.5	70.00	69.27	+0.75	>	Battery supplies the 2WDSEV (discharging battery)
2	40	1.5	2.5	69.27	69.25	+0.02	>	Battery supplies the 2WDSEV(discharging battery).
	40	2.5	3.0	69.25	69.28	−0.03	<	Solar PV: the solar PV shares its power between the battery and the 2WDSEV (charging the battery).
3	0	3.0	4.5	69.28	69.47	−0.19	<	Solar PV: the solar PV shares its power between the battery and the 2WDSEV (charging the battery).

Table 8.
PV array parameters.

Module: Sun Power SPR-X20-445-COM			
Parallel string	6	Cells per module	128
Series connected	3	Short-circuit (A)	6.21
Maximum power (W)	444.86	Current at maximum power point (A)	5.8
Open circuit voltage (V)	90.5	Temperature coefficient of Isc(%/°C)	0.013301
Voltage at maximum power point (V)	76.7	Light-generated current I_L(A)	6.2167
Temperature coefficient of Voc(%/°C)	−0.29101	Diode saturation current I_0(A)	1.3552e-11
Diode ideality factor	1.026	Series resistance Rsh(Ω)	508.2463
Series resistance R_s(Ω)	0.54861		

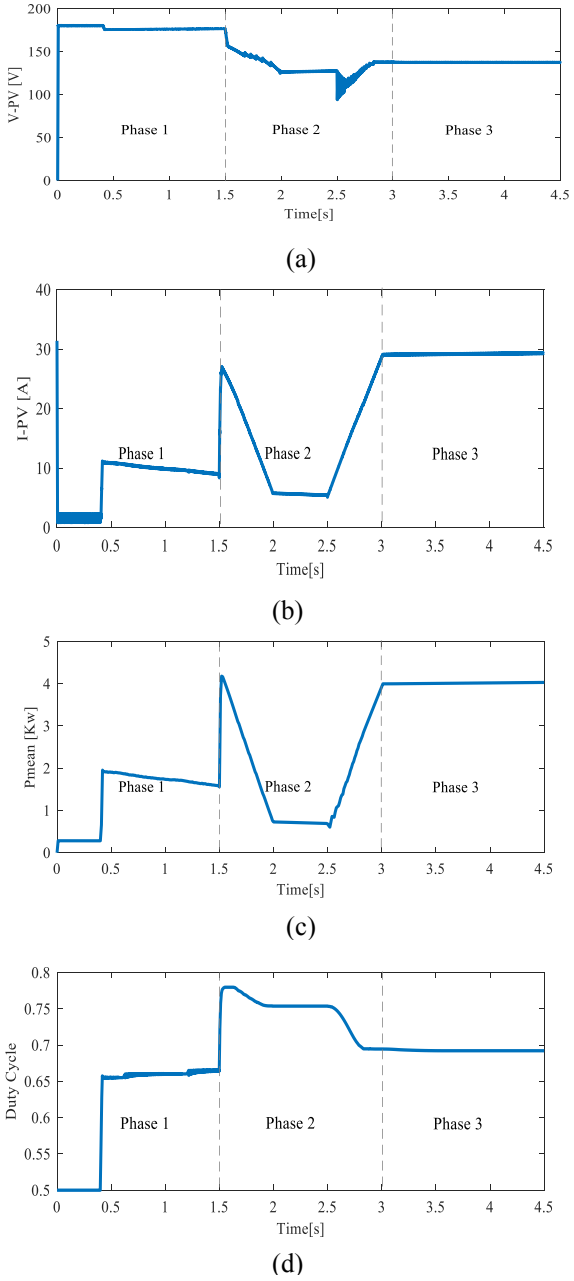

Fig. 14. PV parameters at different speed variations; (a): PV v oltage; (b): PV current; (c): power mean; (d): duty cycle.

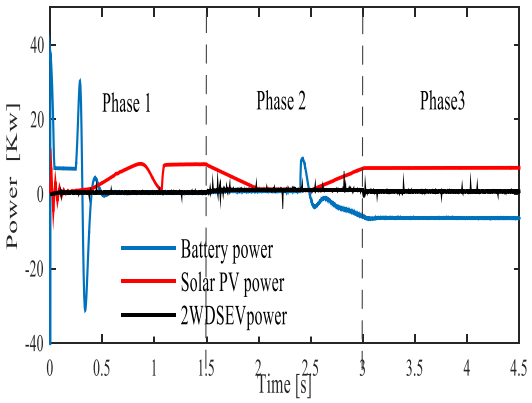

Fig. 15. NiMH battery, solar PV, and SEV power, respectively, at different speeds.

Figure 15 summarizes the results in two parts. The first part is the discharge mode, when the power of the battery took a positive value and covered vehicle consumption due to low solar PV power output; this began at t = 0–2 s. At t = 2.5 s, the solar PV began to feed the vehicle as the battery power took a negative value as it began to charge.

6. Conclusions

The vehicle energy policy outlined in this paper has demonstrated that hybrid power sources based on a solar PV panel and a NiMH battery controlled by a buck boost DC–DC converter, used in an SEV that utilized two rear driving wheels for motion, can be improved using an artificial neural network-based direct torque control strategy when the developed power depended on the driver's reference speed.

The road topologies and variations in temperature and solar radiation did not affect the performance of the proposed system. The boost DC–DC converter, bidirectional bridge converter output voltage, and the control strategy demonstrated satisfactorily dynamic characteristics vis-à-vis the SEV's propulsion system.

Table 9.
Variations of the sequences of events during the different phases.

Phases	Begin Phase 1 (s)	End Phase 1 (s)	Begin Phase 2 (s)	End Phase 2 (s)	Begin Phase 3 (s)	End Phase 3 (s)	Observations
	0	1.5	1.5	3	3	4.5	
Temperature (C°)	25	25	25	50	50	50	Battery supply the 2WDSEV(discharging battery)
Solar radiation (W/m²)	1000	1000	190	190	1000	1000	
PV voltage (V)	240		220		220		
Mean power PV (kW)	8.00		1.20		7.00		
Duty cycle	0.5	0.35	0.35	0.51	0.51	0.51	

The proposed adaptive fuzzy PI speed controller model improved the wheels' speed control with high accuracy on a flat road. This hybrid power source increased the SEV's autonomy. This study enables the prediction of a hybrid power source's dynamic behavior under different speed variation conditions, which is considered as a foundation for control and power management for two and four rear-wheel drive SEVs.

Acknowledgements

The authors would like to acknowledge, with warm thanks, the Smart Grid and Renewable Energy (SGRE) and the Laboratory of Sustainable Development and Computer Science (LDDI) for their kind cooperation and support.

References

Allaoua, B., Mebarki, B., & Laoufi, A. (2013). A robust fuzzy sliding mode controller synthesis applied on boost DC-DC converter power supply for electric vehicle propulsion system. *International Journal of Vehicular Technology*, 2013; https://doi.org/10.1155/2013/587687

Ammari, C., Hamouda, M., & Makhloufi, S. (2017). Sizing and optimization for hybrid central in South Algeria based on three different generators. *International Journal of Renewable Energy Development*, 6(3), 263-272.

Belatrache, D., Bentouba, S., & Bourouis, M. (2017). Numerical analysis of earth air heat exchangers at operating conditions in arid climates. *International journal of hydrogen energy*, 42(13), 8898-8904; https://doi.org/10.1016/j.ijhydene.2016.08.221

Brahim, G., & Abdelfatah, N. (2012). A novel 4WD electric vehicle control strategy based on direct torque control space vector modulation technique. *Intelligent Control and Automation*, 2012.

Chiu, H. J., & Lin, L. W. (2006). A bidirectional DC–DC converter for fuel cell electric vehicle driving system. *IEEE Transactions on Power Electronics*, 21(4), 950-958; doi: 10.1109/TPEL.2006.876863

Devi, S. R., Arulmozhivarman, P., Venkatesh, C., & Agarwal, P. (2016). Performance comparison of artificial neural network models for daily rainfall prediction. *International Journal of Automation and computing*, 13(5), 417-427; https://doi.org/10.1007/s11633-016-0986-2

Gao, M., & He, S. (2008, October). Self-adapting fuzzy-PID control of variable universe in the non-linear system. *In 2008 International Conference on Intelligent Computation Technology and Automation (ICICTA)* (Vol. 1, pp. 473-478). IEEE.

Gasbaoui, B., Nasri, A., Laoufi, A., & Mouloudi, Y. (2013). 4 WD Urban Electric Vehicle Motion Studies Based on MIMO Fuzzy Logic Speed Controller. *International Journal of Control and Automation*, 6(1), 105-118.

Javed, K., Ashfaq, H., & Singh, R. (2018). An Improved MPPT Algorithm to Minimize Transient and Steady State Oscillation Conditions for Small SPV Systems. *International Journal of Renewable Energy Development*, 7(3). doi.org/10.14710/ijred.7.3.191-197

Kumar, C. H., & Rao, R. S. (2016). A novel global MPP tracking of photovoltaic system based on whale optimization algorithm. *International Journal of Renewable Energy Development*, 5(3); https://doi.org/10.14710/ijred.5.3.225-232

Mebarki, B., Allaoua, B., Draoui, B., & Belatrache, D. (2017). Study of the energy performance of a PEM fuel cell vehicle. International *Journal of Renewable Energy Research (IJRER)*, 7(3), 1395-1402.

Moreno, J., Dixon, J., & Ortuzar, M. (2006). "Energy management system for an electric vehicle, using ultra capacitors and neural networks. *IEEE Transactions on Industrial Electronics*, 53(2), 614-623.

Ouledali, O., Meroufel, A., Wira, P., & Bentouba, S. (2019). Genetic Algorithm Tuned PI Controller on PMSM Direct Torque Control. *Algerian Journal of Renewable Energy and Sustainable Development*, 1(2), 204-211. doi.org/10.46657/ajresd.2019.1.2.10

Prelas, M. A. (2009). *Energy Resources and Systems: Volume 1: Fundamentals and Non-Renewable Resources*. Springer Netherlands.

Reddy, Y. S., Vijayakumar, M., & Reddy, T. B. (2007). Direct torque control of induction motor using sophisticated lookup tables based on neural networks. *AIML Journal*, 7(1), 9-15.

Sasikumar, S., & Harinandan, L. (2014). Automatic power management and monitoring system for electric vehicles. *Int. J. Technol. Enhancem. Emerging Eng. Res*, 2(4), 134-137.

Shen, J. M., Jou, H. L., Wu, J. C., & Wu, K. D. (2014). Single-phase three-wire grid-connected power converter with energy storage for positive grounding photovoltaic generation system. *International Journal of Electrical Power & Energy Systems*, 54, 134-143; https://doi.org/10.1016/j.ijepes.2013.07.002

Tahiri, F., Bekraoui, F., Boussaid, I., Ouledali, O., & HARROUZ, A. (2019). Direct Torque Control (DTC) SVM Predictive of a PMSM Powered by a photovoltaic source. *Algerian Journal of Renewable Energy and Sustainable Development*, 1(01), 1-7; https://doi.org/10.46657/ajresd.2019.1.1.1

Yang, Y. P., & Lo, C. P. (2008). Current distribution control of dual directly driven wheel motors for electric vehicles. *Control Engineering Practice*, 16(11), 1285-1292; https://doi.org/10.1016/j.conengprac.2008.02.005

Zhang, Q., & Yin, Y. (2003). Analysis and evaluation of bidirectional DC/DC converter. Journal of Power Technology, 1(4), 331-338;